

Influence of normal stress and grain shape on granular friction: Results of discrete element simulations

Yonggui Guo and Julia K. Morgan

Department of Earth Science, Rice University, Houston, Texas, USA

Received 24 June 2004; revised 30 September 2004; accepted 6 October 2004; published 17 December 2004.

[1] Laboratory experiments of granular shear deformation demonstrate that loading conditions and grain characteristics can significantly affect the macroscopic friction of a granular material under shear. We have examined the variation of maximum sliding friction with normal stress and grain shape using a version of the distinct element method (DEM) that includes bonds between adjacent particles. In this way, arbitrarily shaped grains can be generated to reproduce more realistic fault gouge with a range of grain sizes and shapes. Two types of grains were designed to represent quartz gouge: rounded grains composed of seven close-packed particles and triangular grains composed of six close-packed particles. DEM experiments were conducted by shearing granular assemblages with different grain shape distributions using the identical boundary configurations (i.e., wall surface roughness) over a range of normal stresses from 5 to 100 MPa and were compared to equivalent experiments using reference circular particle assemblages. The results show an inverse power law relationship between normal stress and maximum sliding friction in all cases, where both its coefficient and exponent are dependent on gouge angularity. Under normal stress over 20 MPa, triangular grain assemblages exhibited the highest frictional strength and also the highest abundance of rotating grains, demonstrating that enhanced grain rolling alone does not explain the low frictional strength of simulated granular assemblages. *INDEX TERMS*: 3210 Mathematical Geophysics: Modeling; 5104 Physical Properties of Rocks: Fracture and flow; 7209 Seismology: Earthquake dynamics and mechanics; 8010 Structural Geology: Fractures and faults; *KEYWORDS*: granular friction, DEM simulations, normal stress, grain shape, discrete element method, granular shear

Citation: Guo, Y., and J. K. Morgan (2004), Influence of normal stress and grain shape on granular friction: Results of discrete element simulations, *J. Geophys. Res.*, 109, B12305, doi:10.1029/2004JB003044.

1. Introduction

[2] Frictional sliding of brittle shear zones at shallow depth is commonly accompanied by production, accumulation, and evolution of noncohesive wear detritus with angular forms called fault gouge. It has long been recognized that the presence of fault gouge has significant effects on the mechanical behavior of fault zones [Byerlee, 1967; Byerlee and Summers, 1976; Scholz et al., 1972], and the stability of natural faults [Scholz et al., 1969; Marone and Scholz, 1988]. Therefore a full understanding of fault strength, dynamic behavior, and earthquake mechanisms requires a complete knowledge of the frictional properties of fault gouge under a wide range of conditions.

[3] A considerable body of experimental work has been carried out to identify the effects of a variety of gouge materials on frictional behavior of fault zones under various experimental conditions. Early work was focused on the effects of gouge on base level rock friction, as the production of gouge during slip of initially bare rock

surfaces was found to result in a decrease in frictional resistance [e.g., Byerlee, 1967; Scholz et al., 1972]. Studies on gouge rock friction [Engelder et al., 1975; Byerlee et al., 1978; Logan et al., 1979; Moore et al., 1988; Tullis et al., 1989] indicated that the accumulation of gouge, and development of shear localization features within gouge, may influence fault constitutive behavior and stability of sliding. Further studies [Dieterich, 1979; Ruina, 1983; Rice and Ruina, 1983; Chester and Higgs, 1992; Reinen et al., 1994; Perrin et al., 1995] demonstrated that second-order variations in friction of simulated fault zones can be described by several constitutive laws in terms of slip rate and state of the frictional shear zone. The Dieterich-Ruina rate/state constitutive law, currently in best agreement with experimental results [Beeler et al., 1994; Nakatani, 2001], provides the basis for predicting the frictional response to a change in slip rate (i.e., velocity strengthening and velocity weakening).

[4] To validate and constrain the constitutive laws for frictional evolution under a wide range of conditions, laboratory experiments investigating the effects of variations in extrinsic factors on the frictional strength of simulated fault gouge have been carried out. These factors

include normal load [Linker and Dieterich, 1992; Richardson and Marone, 1999], shear load [Nakatani and Mochizuki, 1996; Nakatani, 1998; Karner and Marone, 1998; Olsen et al., 1998], loading velocity [Mair and Marone, 1999], normal stress (σ_n) vibrations [Richardson and Marone, 1999], shear load perturbations [Karner and Marone, 2001], shear displacement [Beeler et al., 1996], and hydrothermal conditions [Karner et al., 1997]. These studies have led to empirical descriptions of friction in terms of the various extrinsic factors. Nonetheless, none of existing friction laws can completely describe the observed frictional behavior of fault gouge, due in part to the complexity and evolution of the topography of the contacting surfaces [e.g., Karner and Marone, 1998; Richardson and Marone, 1999; Karner and Marone, 2001]. Recently, attention has been focused on the influences of various intrinsic factors, such as mineralogy [Olsen et al., 1998; Saffer et al., 2001], grain shape, size, size distribution, and surface roughness [Mair and Marone, 2000; Frye and Marone, 2002; Mair et al., 2002], on shear zone strength and sliding behavior. As an example of these influences, recent investigations have demonstrated that the coefficient of sliding friction for gouge made of spherical glass beads is markedly lower than for angular quartz sand [Mair et al., 2002].

[5] Laboratory experiments have made significant advances in understanding the effects of gouge on rock friction, but as shown above, the underlying micromechanical processes of these effects remain elusive. Poor understanding of the micromechanics of gouge deformation has obviously impeded the development of the next generation of constitutive laws built upon a micromechanical framework to quantitatively interpret friction data. With laboratory experiments, it is difficult to set up experiments under identical boundary conditions in order to directly correlate variations in gouge friction to variations of extrinsic factors, intrinsic factors, and corresponding deformation mechanisms during simulated gouge deformation. Therefore many important problems related to micromechanics of gouge cannot be fully addressed by current laboratory experiments. For example, outstanding questions include how deformation is partitioned among mechanisms such as grain rolling, sliding, and fracturing, and how deformation mechanisms affect both base level and second-order frictional strength of fault gouge, and evolve with grain size, shape, size distribution, configuration, and microstructure.

[6] Numerical simulations of the frictional behavior of fault zones represent an alternative approach for exploring micromechanisms of shear zone deformation, and offer an outstanding opportunity to extend our knowledge of fault mechanics beyond the domain accessible to laboratory observations [Mora and Place, 1998, 1999; Morgan and Boettcher, 1999; Morgan, 1999; Place and Mora, 2000]. Unlike many continuum numerical models based on the macroscopic and continuous media in which rheology is assumed in advance (i.e., intrinsic properties are averaged) [Day, 1982; Fukuyama and Madariaga, 1995; Madariaga et al., 1997; Tang, 1997], the distinct element method (DEM) [Cundall and Strack, 1979] provides a way to study the dynamic behavior of discontinuous granular materials, and therefore fault gouge, as a function of intrinsic variables and contact physics. This technique has been successfully employed to reproduce characteristic shear fracture

arrays commonly observed in naturally and experimentally deformed gouges [Morgan and Boettcher, 1999].

[7] One limitation in many of the recent DEM simulations, however, has been the use of circular gouge grains. Base friction values obtained from two-dimensional (2-D) DEM simulations are about 0.3 [e.g., Morgan, 1999], significantly lower than the base level friction predicted by Byerlee's law, raising concerns that the simulations represent nonphysical results. Laboratory experiments carried out on real materials with equally simple 2-D geometries, e.g., quartz rods and even pasta, however, have yielded remarkably similar friction data to numerical simulations of 2-D circular particles, thereby confirming the first-order DEM friction values [Frye and Marone, 2002]. Further idealized laboratory studies of 3-D spherical particles have demonstrated slightly higher friction values, approaching 0.45, but also show that friction increases with particle angularity [Mair et al., 2002]. These laboratory results serve to validate the DEM simulations, but show that circular particles are too simple to represent real fault gouge. Natural fault gouge is usually composed of angular-shaped grains that are thought to exhibit significantly less grain rolling and more grain interlocking than particle dynamics simulations [Mora and Place, 1998, 1999; Morgan and Boettcher, 1999; Mair et al., 2002]. Here, we further our understanding of the role of particle angularity on the first-order friction value by considering irregularly shaped grains with different abundances within simulated fault gouge.

[8] Laboratory experiments on angular sand also show that σ_n plays an important role in the development of microstructures in fault gouge by controlling the active deformation mechanisms, i.e., rolling and sliding dominant at nonfracture regime, and fracture and grain size reduction more active at higher normal stresses [Mair et al., 2002]. The results suggest that active deformation mechanisms are not only dependent on grain shape but also on σ_n . Therefore σ_n may also lead to additional variations of friction. In fact, second-order effects on friction associated with variations in σ_n have been shown to produce a decreasing trend in friction observed in many laboratory experiments [e.g., Maurer, 1965; Murrell, 1965; Byerlee, 1967, 1968; Handin, 1969; Jaeger, 1970; Edmond and Murrell, 1971; Saffer et al., 2001; Saffer and Marone, 2003], but the dependency of friction on σ_n has not been well studied in previous numerical simulations on rock friction. As it is often difficult to conduct laboratory experiments under the exact same conditions to examine the effect of a single variable on the variation of rock friction, numerical experiments can provide a better understanding of effect of σ_n on active deformation mechanisms and friction.

[9] In order to study the variation of frictional strength and dynamic behavior of fault zones as a result of changing grain shape and σ_n , we carry out DEM simulations using grains constituted of bonded circular particles under a range of normal stresses from 5 to 100 MPa. In this way, arbitrarily shaped grains can be generated to reproduce more realistic fault gouge morphology, and we can quantify the effects of gouge grain shape and σ_n on the friction of simulated granular assemblages. Simulations are carried out in 2-D for comparison with previous modeling studies. The results show that angular grain assemblages are stronger than rounded grain assemblages, as observed in laboratory

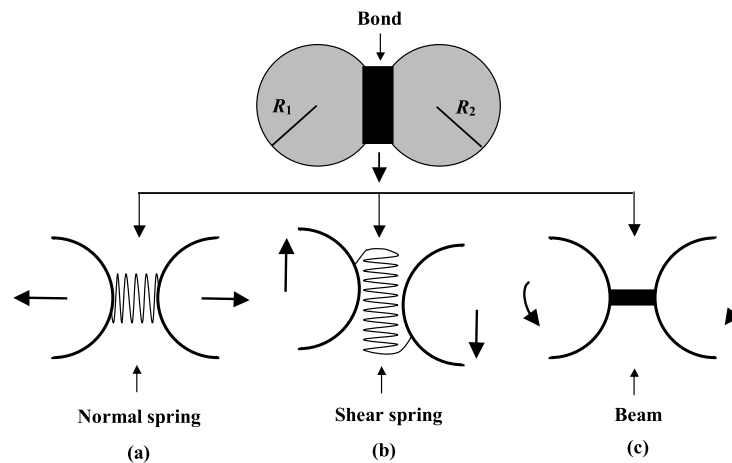


Figure 1. Schematic diagram of interparticle bond and its mechanical analogs. The bond between particles behaves as (a and b) two elastic springs that generate and transmit normal and shear forces, respectively, and (c) an elastic beam that transmits moment.

experiments of 3-D materials [Mair *et al.*, 2002]. Frictional strength of simulated granular assemblages increases non-linearly with decreasing σ_n , and follows an inverse power law that is identical in form to a theoretical friction law based on Hertzian contact model [Bowden and Tabor, 1964; Jaeger and Cook, 1976; Villaggio, 1979]. The decreasing trend of sliding friction with increasing σ_n is comparable to recent laboratory observations [Saffer *et al.*, 2001; Saffer and Marone, 2003]. Grain shape irregularity is also observed to affect the strength of granular assemblages. It determines the rate of change in friction by increasing both the coefficient and exponent of the friction law. Our results demonstrate that DEM simulations can appropriately represent the characteristic mechanical behavior of irregular granular gouge, bringing us one step closer to understanding the micromechanics of fault slip and friction.

2. Experimental Method

2.1. The Distinct Element Method

[10] The distinct element method (DEM) [Cundall and Strack, 1979] is a numerical technique that was initially proposed as a new tool to investigate the mechanical behavior of assemblies of discs and spheres as analogs of soil, rock, or industrial materials. The principles on which DEM is based have been described very well by others [Cundall and Strack, 1979; Antonellini and Pollard, 1995; Morgan and Boettcher, 1999; Burbidge and Braun, 2002]. It has been shown that this technique is a suitable tool for modeling real granular materials, such as sand and fault gouge [Cundall and Hart, 1992; Morgan and Boettcher, 1999; Morgan, 1999]. Although most DEM simulations were carried out in two dimensions, the technique can be also used to simulate 3-D assemblages at higher computational expense [e.g., Hazzard and Mair, 2003]. Previous DEM simulations have been limited in several ways: lack of grain fracture; use of circular or spherical particles; and lack of evolution of grain shape and size during the simulations. In contrast, in natural systems, highly angular particles undergo pervasive fracture and comminution during faulting and shearing [Sammis *et al.*, 1987; Marone and Scholz, 1989; Mair *et al.*, 2002]. Ultimately, these limitations need

to be overcome in order to simulate the shear zone deformation in a more realistic way.

[11] As a first step, we examine role of grain shape on base level friction of granular shear zones maintaining 2-D geometry for computational efficiency. In order to build angular grains, we introduce interparticle bonds. Various numerical models [Zubelwicz and Bazant, 1987; Plesha and Aifantis, 1983; Trent, 1987; Iwashita and Hakuno, 1990; Bruno and Nelson, 1991; Bojtár and Bagi, 1993; Donzé and Magnier, 1995; Jirásek and Baant, 1995] have been proposed to simulate breakable interparticle bonds and grain fracture. Here, we have incorporated a linear elastic particle bond model into DEM for the purpose of generating arbitrary-shaped grains in this paper, and eventually, for simulating fracture during granular shear (e.g., Y. Guo and J. K. Morgan, manuscript in preparation, 2004). The method builds on a bond model used in the Particle Flow Code in 2-Dimensions [Itasca Consulting Group, 1999] with some necessary modifications as described below.

[12] In our model, two bonded particles are assigned a zero separation when the bond is formed, defining a zero force configuration. Dynamically, the bond between particles behaves as two elastic springs (normal and shear) (Figures 1a and 1b) and an elastic beam (Figure 1c). The normal spring, with normal stiffness k_n , produces and transmits a restoring normal force (both tensile and compressive). The shear spring, with shear stiffness k_s , produces and transmits a restoring shear force. The beam transmits a moment if a relative rotation occurs between the two bonded particles. The interparticle bonds are assumed to deform in a linear elastic manner within a predefined failure criterion for each mode, as the bonded particles are displaced and rotated from their equilibrium positions. Forces and moment within the elastic bond are proportional to bond stiffness and bond cross-sectional area and therefore can be calculated from the known displacements by

$$\mathbf{F}_n = k_n A \cdot \delta_n \quad (1)$$

$$\mathbf{F}_s = k_s A \cdot \delta_s \quad (2)$$

$$\mathbf{M} = k_n I \cdot \theta \quad (3)$$

where \mathbf{F}_n , \mathbf{F}_s , and \mathbf{M} are the normal force, shear force, and moment within the bond, respectively; δ_n , δ_s , and θ are the relative normal, shear, and angular displacements at the particle contact, respectively. Both the cross-sectional area of the bond, A , defined at bond formation, and the moment of inertia of the bond cross section, I , are a function of the effective radius of the bond cross section R and are defined as

$$A = \pi R^2 \quad (4)$$

$$I = \frac{1}{4}AR^2 \quad (5)$$

R is determined by the radius of two contact particles R_1 and R_2 and given by

$$R = \frac{2R_1R_2}{R_1 + R_2} \quad (6)$$

[13] By assuming that tensile normal force is positive, the normal stress (both tensile and compressive) and shear stress acting on the bond can be defined as

$$\sigma = \frac{\mathbf{F}_n}{A} + \frac{|\mathbf{M}|}{I}R \quad (7)$$

$$\tau = \frac{|\mathbf{F}_s|}{A} \quad (8)$$

[14] For the case of unbonded particles in contact, contact force is described using the nonlinear Hertz-Mindlin contact model [Mindlin and Deresiewicz, 1953; Johnson, 1985]

$$\mathbf{F}_n = \left(\frac{2G\sqrt{2R}}{3(1-\nu)} \right) \delta_n^{3/2} \quad (9)$$

$$\mathbf{F}_s = \left(\frac{2[3RG^2(1-\nu)]^{1/3}}{(2-\nu)} \right) \mathbf{F}_n^{1/3} \quad (10)$$

where G is the shear modulus and ν is Poisson's ratio (Table 1).

2.2. Experimental Design

[15] The major purpose of this paper is to examine the influence of σ_n and grain shape on the sliding friction of sheared granular assemblages. In order to study the effect of grain shape on sliding friction, we generated five different grain assemblages by proportionally distributing two different types of grains: rounded grains composed of seven close-packed circular particles of equal size, and triangular grains composed of six close-packed circular particles of equal size (Figure 2b). The grain assemblages contained different percentages of triangular grains, i.e., 0%, 25%, 50%, 75%, or 100%, defined by grain abundance. Four different grain sizes were created by bonding particles of four different radii, given as 100, 117.6, 138.4, and 162.8 μm . As grain size distribution during shear zone deformation evolves through cataclasis toward a power

Table 1. Parameters for Numerical Experiments

Parameter	Value
Experimental variables	
Initial gouge zone thickness ^a	~ 11.25 mm
Shear strain rate ^a	$\sim 8.89 \times 10^{-5}$
Total shear strain	200%
Applied normal stress on walls	5–100 MPa
Grain properties	
Grain radius	300, 352.9, 415.2, and 488.5 μm
Exponent for grain size distribution (D) (see equation (11))	0.51
Grain shape distribution (S) ^b	100% (T000) 75% (T025) 50% (T050) 25% (T075) 0% (T100)
Interparticle friction	0.5
Shear modulus	29 GPa
Poisson's ratio	0.20
Interparticle bond properties	
Poisson's ratio	0.20
Young's modulus	69.6 GPa
Maximum tensile strength	∞^c
Maximum shear strength	∞^c

^aDepend on normal stress and grain shape.

^b S represents the degree of grain angularity quantified by the percentage of the triangular grains. For convenience, we use T100, T075, T050, T025, and T000 to represent five granular assemblages, respectively. T represents triangular grain and the number behind it is the percentage of the triangular grains.

^cPrevents grain fracture.

law distribution [Sammis *et al.*, 1986, 1987], the relative abundances of four different sized grains satisfy this law. The power law is defined with a fractal dimension D and given by the following relationship [Turcotte, 1986; Sammis *et al.*, 1986, 1987; Morgan and Boettcher, 1999]:

$$D = \log(N_i/N_0) / \log(R_0/R_i) \quad (11)$$

where N_i and N_0 are numbers of grains with a radius equal to R_i and R_0 , respectively (Table 1). The value of D in our assemblages is held constant at 0.51.

[16] A reference circular particle assemblage with D value of 0.51 (Figure 2a) was created by randomly arranging a predetermined number of circular particles of four sizes within the domain with periodic boundaries that were moved inward until the isotropic mean stress was attained. There are about 16 particles in a vertical column of the circular particle assemblage. The initial grain assemblage (Figure 2b) was created by proportionally replacing circular particles of same size with rounded and/or triangular grains between two rough-surfaced walls. Only rounded grains are used within the walls so that wall surface roughness is the same for all grain assemblages. By maintaining constant wall surface roughness, initial grain configuration (i.e., positions), and grain size distribution for all the experiments, we can isolate the specific effects of grain angularity and normal stress. Before the start of the experiment, the granular assemblage was compacted by shifting the top wall back and forth under the applied experimental normal stress until the equilibrium stress and porosity (Table 2) were reached. The granular assemblage was then deformed by moving the upper wall at constant velocity to the right, while keeping the lower wall fixed. The constant wall

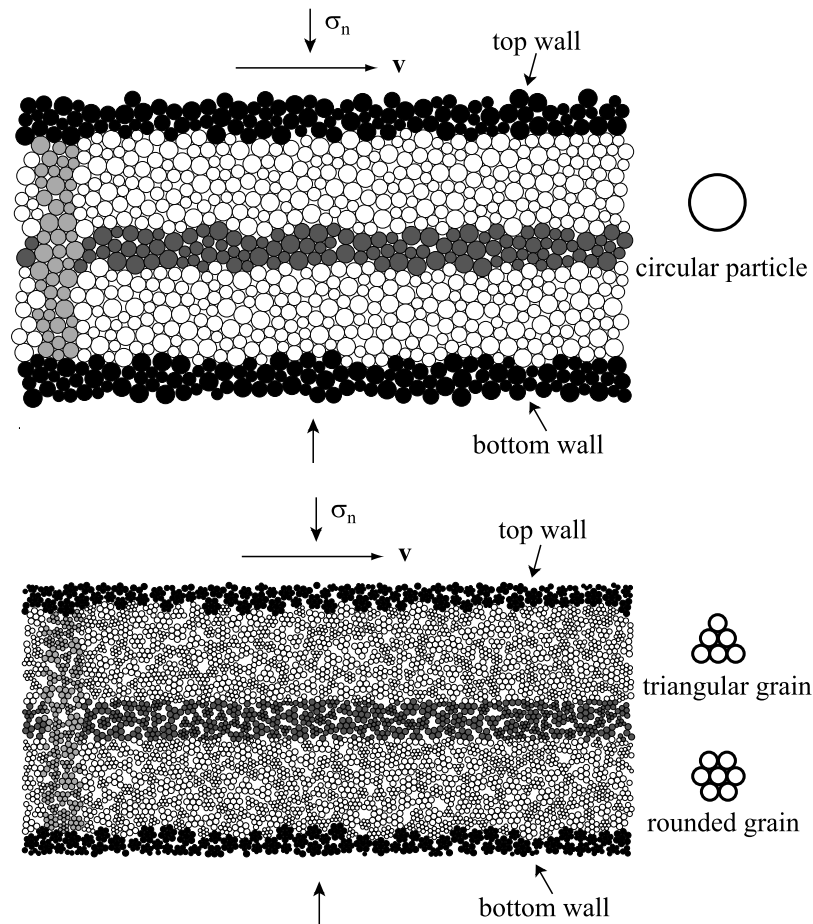


Figure 2. Experimental design. (a) Initial reference assemblage of circular particles with D value of 0.51, created by randomly arranging a predetermined number of circular particles of four sizes within the domain with periodic boundaries. Boundaries were moved inward until equilibrium isotropic mean stress was attained. (b) Initial grain assemblage created by replacing circular particles of same size with rounded and/or triangular grains in certain proportions. Rounded grains define two rough-surfaced walls for all grain assemblages. Normal stress was maintained at a constant value throughout each experiment. Deformation was induced by moving top wall to the right at a constant velocity, v , and keeping bottom wall fixed. Shaded vertical and horizontal columns are strain markers.

velocity condition equates to infinite wall stiffness, precluding velocity variations associated with the stick-slip deformation. Data on grain displacements and interactions were recorded after each 2% shear strain increment.

[17] For the purpose of investigating the variation of sliding friction due to σ_n and grain shape, the DEM experiments for each of the five grain assemblages with different grain shape characteristics were carried out under identical boundary conditions (i.e., wall surface roughness and strain rate are the same for all experiments) over a range of normal stresses, i.e., 5, 25, 50, 75, and 100 MPa. For comparison, we also carried out a similar suite of numerical experiments using unbonded, circular particles with the same size and size distribution as the rounded grains. Parameters for the numerical experiments are listed in Table 1.

3. Results

[18] In this study, friction of the granular assemblage is defined as the ratio of shear stress to normal stress, i.e.,

$\mu = \tau/\sigma_n$. As σ_n is held constant during a given experiment, μ serves as a normalized measure of shear stress. The typical friction versus shear strain curve of our numerical experiments is characterized by a peak friction, defined as μ_{peak} , reached within the first 40% shear strain and followed by a gradual decrease over about 10% shear strain. Friction then fluctuates about a residual value,

Table 2. Equilibrium Porosity for Granular Assemblages of Different Grain Composition Sheared Under Various Normal Stresses

Experiment	Normal Stress, MPa				
	5	25	50	75	100
T100	0.602	0.593	0.582	0.573	0.57
T075	0.593	0.578	0.566	0.56	0.553
T050	0.57	0.565	0.553	0.546	0.542
T025	0.566	0.547	0.54	0.534	0.528
T000	0.533	0.528	0.523	0.519	0.516
C100	0.455	0.443	0.435	0.43	0.426

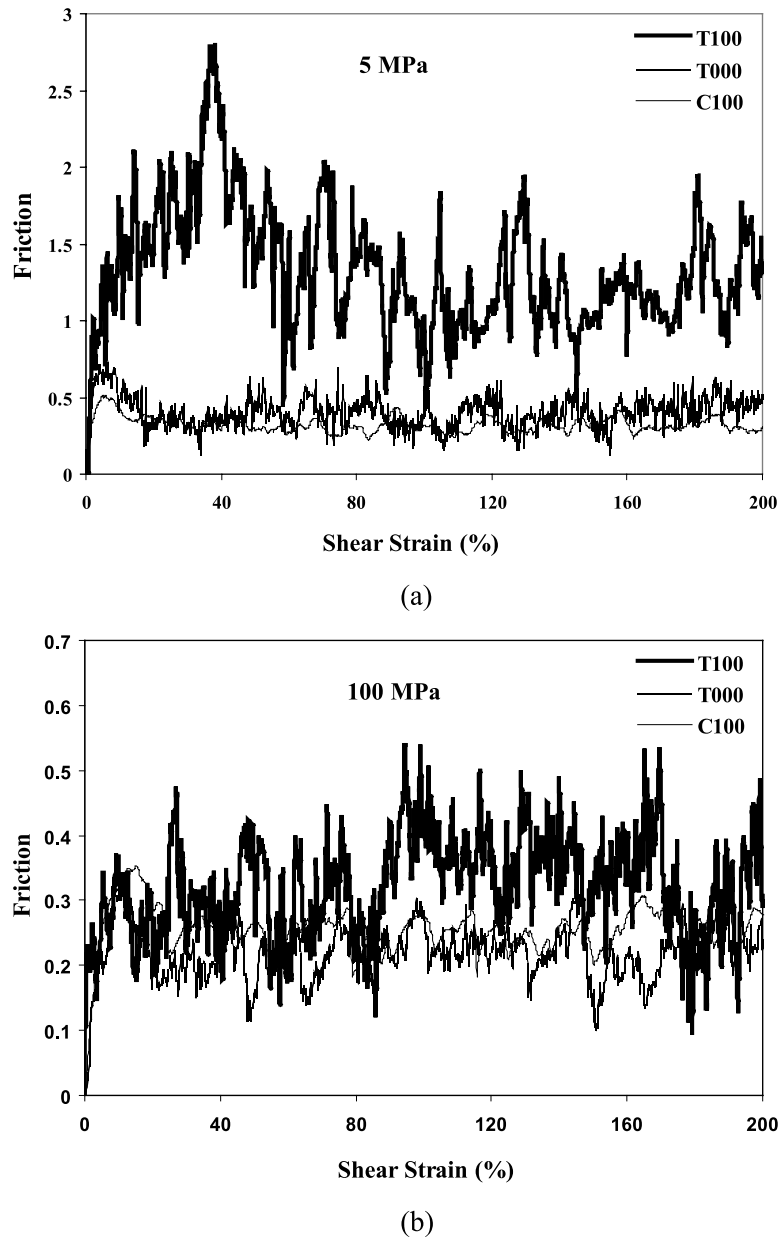


Figure 3. Friction data for granular assemblages composed of different shaped grains under (a) low and (b) high normal stresses. Frictional behavior of the rounded grain assemblage (T000) is similar to the circular particle assemblage (C100). The triangular grain assemblage (T100) is much stronger than the other two.

defined as μ_{mean} (Figure 3). The fluctuations in friction arise from stress averaging over the small number of particles in the assemblage, as well as heterogeneous interactions along the irregular shear zone walls. The amplitude of friction fluctuations generally decreases with increasing particle abundance [e.g., Morgan, 1999], approaching the smooth friction trends observed in laboratory experiments in the absence of stick-slip behavior [e.g., Mair *et al.*, 2002]. Since all of the sheared assemblages begin to slide steadily by 60% shear strain, we refer to the friction after 60% strain increments as sliding friction in order to distinguish from μ_{peak} . Maxi-

imum sliding friction μ_{max} , representative of the shear strength of the assemblage, is calculated as the sum of μ_{mean} and its standard deviation. Data on frictional and micromechanical properties of the granular assemblage were recorded at every 2% shear strain. Again, only the data after 60% shear strain were used for the analysis of variation μ_{max} and micromechanical properties of granular assemblage.

3.1. Effects of σ_n and Grain Shape on μ_{max}

[19] Both grain shape and normal stress affect the variation of μ_{max} . Representative examples are shown in Figure 3.

Table 3. Maximum Sliding Friction for Granular Assemblages of Different Grain Composition Sheared Under Various Normal Stresses

Experiment	Normal Stress, MPa				
	5	25	50	75	100
T100	1.49	0.709	0.602	0.531	0.411
T075	1.246	0.722	0.424	0.394	0.339
T050	0.864	0.558	0.423	0.312	0.297
T025	0.753	0.459	0.373	0.326	0.287
T000	0.488	0.363	0.306	0.282	0.258
C100	0.37	0.329	0.286	0.283	0.282

Figure 3a plots friction calculated for three assemblages composed of different shaped grains: triangular, rounded, and circular, as a function of shear strain at low σ_n (5 MPa). The rounded grain and circular particle assemblages show similar frictional strength and behavior. However, μ_{peak} and magnitude of fluctuations of the rounded grain assemblage are slightly higher than these of the circular particle assemblage. Variations of friction for both assemblages are similar in form and magnitude to the laboratory experiments on 2-D pasta and quartz rods [Frye and Marone, 2002]. The triangular grain assemblage is markedly stronger than the other two assemblages, reaching μ_{peak} at 2.8 and μ_{max} at 1.49. Variations of friction with shear strain are characterized by longer-period and greater magnitude saw-tooth fluctuations than the rounded grain assemblage, a result of the greater irregularity of particles. For high σ_n (100 MPa) experiments (Figure 3b), friction curves of the rounded grain and circular particle assemblages match each other very well in terms of peak friction and variations in friction with shear strain. The triangular grain assemblage again exhibits higher friction values and large fluctuations in friction compared with the others, but significantly lower than observed at 5 MPa. The results show that both grain shape and σ_n have significant effects on the magnitude of μ_{max} . At low σ_n , μ_{max} of the rounded grain assemblage is

about 0.49, close to results of laboratory experiments conducted on 3-D glass beads under similar conditions [Mair *et al.*, 2002], and decreases to 0.26 when σ_n increases to 100 MPa. The value of μ_{max} for the triangular grain assemblage also decreases with increasing σ_n from 1.49 at 5 MPa to 0.41 at 100 MPa (Table 3). Therefore the effect of grain shape on friction becomes more significant as σ_n decreases.

[20] The variation of sliding friction with both σ_n and grain shape was rigorously quantified by carrying out a series of numerical experiments under a wide range of normal stresses. Specifically, five numerical experiments were conducted at each normal stress by systematically changing the proportion of triangular and rounded grains to constrain the effects of grain shape. Values of μ_{max} are listed in Table 3. For each grain assemblage, μ_{max} decreases nonlinearly with increasing σ_n . At each normal stress, μ_{max} decreases with decreasing proportion of triangular grains. These relationships hold true for all five grain assemblages of different grain shape compositions under all applied experimental stresses. Decreasing trend of μ_{max} with increasing σ_n is also observed for circular particle assemblage but with a lower decreasing rate compared to the grain assemblages. The final results are well fit by inverse power law relationships between μ_{max} and σ_n (Figure 4), and can be expressed by

$$\mu_{\text{max}} = a\sigma_n^{-b} \quad (12)$$

Best fit values of coefficient a and exponent b are listed in Table 4. Both of them tend to increase with increasing gouge angularity.

3.2. Effects of σ_n and Grain Shape on Micromechanical Behavior of Granular Assemblages

[21] Grain assemblages deformed under low σ_n of 5 MPa develop narrow, and high-porosity zones of shear parallel and close to the top wall. Both the gradient of grain

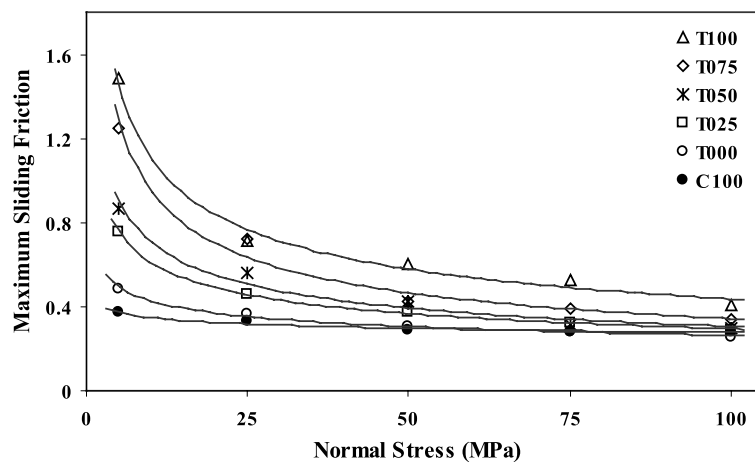


Figure 4. Maximum sliding friction as a function of normal stress for circular particle assemblage and five grain assemblages with different grain shape compositions. The decreasing trends of maximum sliding friction are fitted by inverse power law relationships.

Table 4. Best Fit Values of Coefficient a and Exponent b for Granular Assemblages of Different Grain Composition Sheared Under Various Normal Stresses

Experiment	a	b	R^2
T100	2.8026	0.4037	0.9814
T075	2.6526	0.4448	0.9761
T050	1.6372	0.3644	0.9677
T025	1.2614	0.3159	0.9978
T000	0.6932	0.2098	0.9942
C100	0.4354	0.0979	0.9511

shear displacement (i.e., calculated as the directional derivative of the horizontal grain displacement [e.g., *Morgan and Boettcher*, 1999]), and the distortion of the initially vertical strain marker, denoted by the shaded column of grains (Figures 5b and 5c) show that grain displacement is restricted to this band. At this low σ_n , short-range grain bridges develop readily, supporting the load of the wall (Figures 5a, 5b, and 5c). This leads to high dilation and formation of high pore space near the top wall in all assemblages. Despite the localized shearing, rotating grains are uniformly distributed across the upper half of the rounded grain assemblage (Figure 5b), whereas rotating grains in the triangular grain assemblage are clustered along poorly developed high-angle shear bands (Figure 5c).

[22] In contrast, at high normal stress of 100 MPa, deformation is more distributed throughout the whole domain, and characterized by relative homogeneous pore space and short-lived grain bridges that extend across the domain (Figures 5e and 5f). The high dilation of the assemblage near the top wall at the normal stress of 5 MPa is not observed. The greatest displacements still occur close to the top wall; grains also show the highest rotations in this region. In the rounded grain assemblage, there are a few nonrotating grains close to the bottom wall, while rotating grains are uniformly distributed in the triangular grain assemblage (Figures 5d and 5e). The most distinct differences in deformation state between circular particle assemblage and triangular and rounded grain assemblages are that the circular particle assemblage shows less dilation, lower-porosity, lower abundance of rotating particles, and higher degree of localization (Figures 5a and 5d).

[23] A full understanding of how σ_n and grain shape affect μ_{\max} requires a more complete knowledge of how these factors affect the micromechanical properties of granular assemblages. Statistics on grain rotations, contact sliding, coordination number, and contact force after 60% shear strain demonstrate that σ_n and grain shape have significant influences on these micromechanical properties.

3.2.1. Grain Rotation

[24] The average percentage of rotating grains of each grain assemblage is plotted against σ_n in Figure 6a. The percentage of rotating grains increases with increasing proportion of triangular grains and also with σ_n , except for the rounded grain assemblage. The percentage of rotating grains in the rounded grain assemblage decreases from 74% to 70% with an increase of σ_n from 5 to 25 MPa. Further increase of σ_n does not significantly change the number of rotating grains in the rounded grain

assemblage; this value remains around 70%. The rotational tendency of triangular grains is more sensitive to σ_n , but in the opposite sense. The percentage of rotating grains in triangular grain assemblages increases nonlinearly with increasing σ_n , from 40% at 5 MPa to 91% at 100 MPa. As the percentage of rotating rounded grains changes little with σ_n , this quantity must be mainly controlled by the proportion of triangular grains in assemblages of multiple shaped grains. The percentage of rotating particle in the circular particle assemblage is much lower than the rounded grain assemblage, especially at normal stress of 5 MPa, and decreases with increasing σ_n at normal stresses higher than 25 MPa.

[25] The variations in the average angle of grain rotation with σ_n and grain shape (Figure 6b) show a similar pattern as noted for the percentage of rotating grains. The mean angle of grain rotation does not change significantly with σ_n for the rounded grain assemblage. By comparison, the mean angle of grain rotation in the triangular grain assemblage is lower than that for the rounded grain assemblage at normal stress of 5 MPa, but increases nonlinearly with increasing σ_n . Just as observed with the percentage of rotating grains, a transition occurs at normal stress of 25 MPa. The variations in the mean angle of grain rotation of the other assemblages reflects the combined trends in rotational behavior of the rounded grain and triangular grain assemblages, dependent on the relative abundance of triangular grains (Figure 6b). The mean angle of particle rotation in the circular particle assemblage is smaller than in the rounded grains assemblage and decreases with increasing σ_n .

3.2.2. Contact Sliding

[26] Grain shape has a more significant influence on the percentage of sliding contacts than does σ_n (Figure 7). Yet, the percentage of sliding contacts within all of the grain assemblages does not change as dramatically with σ_n and grain shape as does the percentage of rotating grains. Contacts between triangular grains have a much greater tendency to slide than those between rounded grains. On average, about 15% of the grain contacts slide over each time step in the triangular grain assemblage, whereas only 9% slide in the rounded grain assemblage. The average percentage of sliding contacts in the triangular grain assemblage increases about 1% with increase of σ_n from 5 to 25 MPa, but then shows little change with further increase in σ_n (leveling off at about 15.5%). The percentage of sliding contacts in the rounded grain assemblage decreases steadily from 10.3% to 7.5% as σ_n increases from 5 to 100 MPa. The percentages of sliding contacts of the other grain assemblages decrease with increasing abundance of rounded grains and σ_n . This trend is consistent with variations of sliding contacts in the triangular and rounded grain assemblages. The circular particle assemblage exhibits the similar decreasing trend in the percentage of sliding contacts with increasing σ_n , but less abundance of sliding contact at each normal stress compared to the rounded grain assemblage.

3.2.3. Coordination Number

[27] A plot of average number of contacts per grain, i.e., coordination number, reveals that grain shape strongly influences grain connectivity (Figure 8). Coordination number increases proportionally with increasing abundance

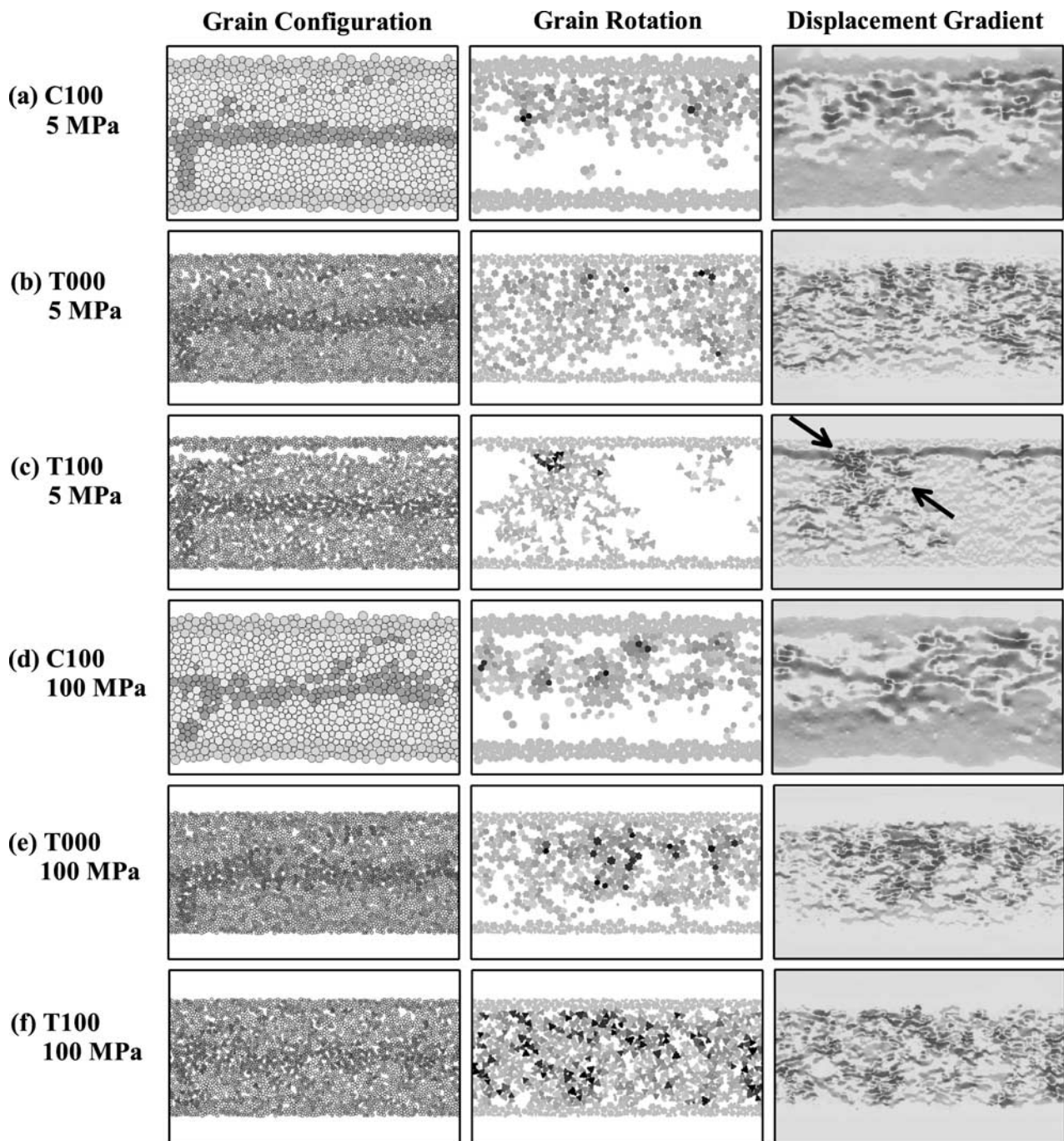


Figure 5. Deformation state of circular particle (C000), rounded grain (T000), and triangular grain (T100) assemblages at low and high normal stresses. (a) Circular particle, 5 MPa; (b) rounded grain, 5 MPa; (c) triangular grain, 5 MPa; (d) circular particle, 100 MPa; (e) rounded grain, 100 MPa; and (f) triangular grain, 100 MPa. (left) Grain configuration. (middle) Grain rotation. Higher degrees of rotation are indicated by darker colors. (right) Gradient of horizontal displacement. Darker colors represent more intense shear strain. See text for discussion. Arrow points to inclined shear band.

of rounded grains. At the same normal stress, coordination number in the rounded grain assemblages is about 20% higher than in the triangular grain assemblages. Variations in coordination number of the other grain assemblages also follow similar trends, i.e., a 25% increment of rounded grains results in about 5% increment in coordination number. Coordination numbers of all the grain assemblages

increase with increasing σ_n , in a very similar pattern: the rate of change in coordination number decreases with increasing σ_n , and coordination number increases about by a factor of 1.6 as σ_n increases from 5 to 100 MPa. Coordination number of the circular particle assemblage also shows an increasing trend with increasing σ_n . It is greater than that of the rounded grain assemblage at normal

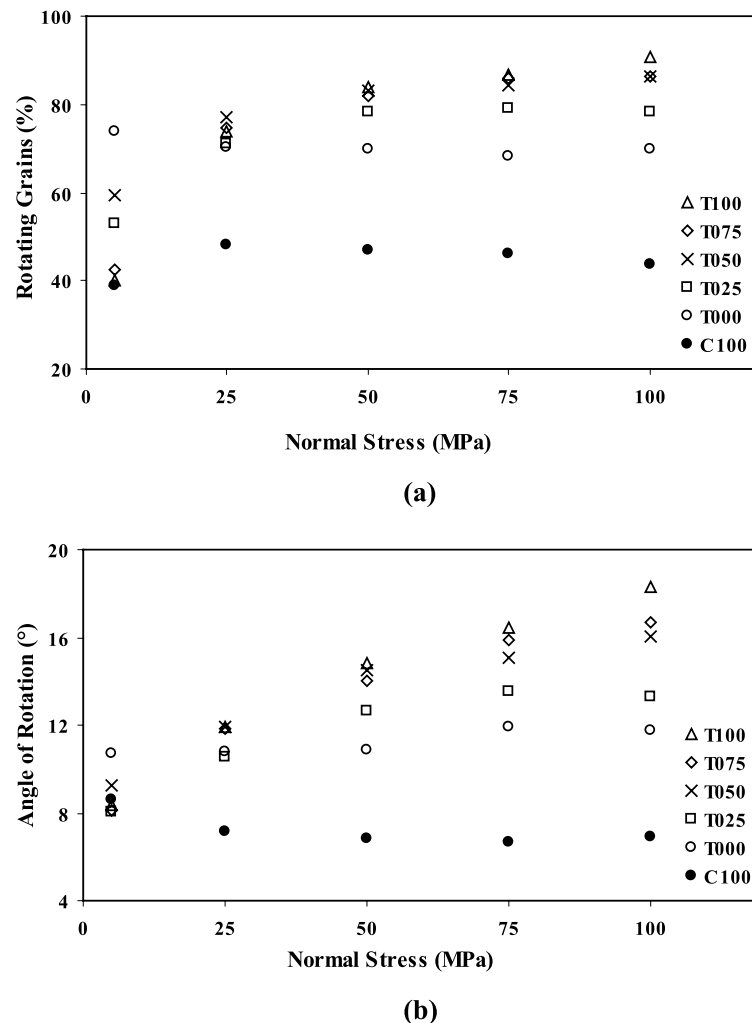


Figure 6. (a) Average percentage of rotating particles or grains for circular particle assemblage and five-grain assemblages of different grain shape composition plotted against normal stress. (b) Average angle of rotation for same assemblages plotted against normal stress. All but the circular particle and rounded grain assemblages show increasing percentage of rotating grains and average angle of rotation with increasing normal stress. Rotation also increases with increasing abundance of triangular grains at normal stresses higher than 5 MPa.

stresses lower than 50 MPa, but becomes slightly smaller at higher normal stresses.

3.2.4. Contact Force

[28] At a given σ_n , the average contact force increases with increasing the abundance of triangular grains. The contact force of the rounded grain assemblage is about 40% lower than that of the triangular grain assemblage at 5 MPa, but only 25% at 100 MPa, even though the absolute difference between the average contact forces increases by more than five times as σ_n increases from 5 to 100 MPa. To study the effect of both σ_n and grain angularity on the variation of contact force, the average contact force of each assemblage at a given σ_n is normalized by the average contact force of that assemblage at normal stress of 100 MPa. A plot of normalized average contact force for each assemblage (Figure 9) demonstrates a nearly linear relationship between σ_n and contact force for all of the assemblages. The normalized average contact forces

increase with increasing σ_n , and their rates of increase are similar and show little dependence on the proportion of rounded and triangular grains (Figure 9).

3.2.5. Volume of Assemblage

[29] Volume changes with increasing σ_n are markedly different for the rounded and triangular grain assemblages. The average volume of each grain assemblage at a given σ_n is normalized by the average volume of that assemblage at normal stress of 5 MPa. In this way, we can document the effects of σ_n on dilation. The normalized volume of the triangular grain assemblage decreases more rapidly than for the rounded grain assemblage with increasing σ_n (Figure 10). The normalized volumes of the mixed rounded and triangular grain assemblages at each normal stress are similar to each other in magnitude, and intermediate to those of the rounded and triangular grain assemblages. The normalized volume of the 75% triangular grain assemblage, which is higher at the normal stress of 25 MPa, decreases

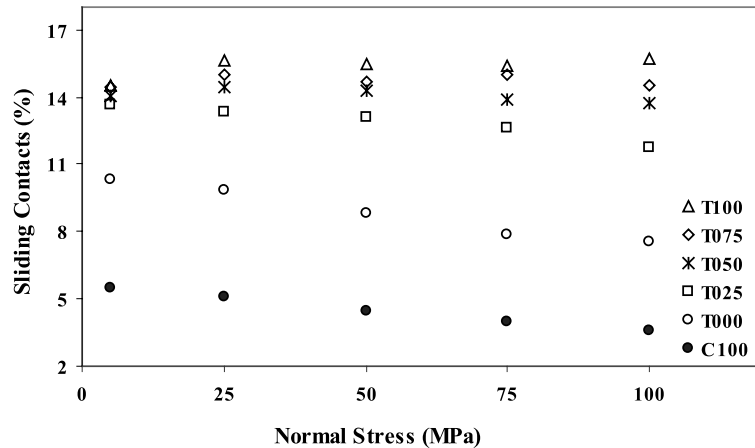


Figure 7. Average percentage of sliding contacts for five granular assemblages of different grain shape composition and one circular particle assemblage plotted against normal stress. The percentages of sliding contacts of all the granular assemblages decrease with decreasing gouge grain angularity and normal stress at normal stress higher than 25 MPa.

more rapidly than the 25% triangular grain assemblage with increasing σ_n . The normalized volume of the assemblage of equal abundance of rounded and triangular grains lies between them. The normalized volume of the circular particle assemblage tends to decrease at a slightly higher rate than the rounded grain assemblage.

4. Discussion

4.1. Maximum Sliding Friction

[30] Variation in friction of faults during sliding is a fundamental factor influencing the generation of earthquakes. Byerlee’s law defines a linear relationship between shear and normal stress, which presumes a constant friction coefficient under normal stress less than 200 MPa [Byerlee,

1978]. This linear friction law can be used to estimate the mean strength of natural faults. However, it neglects important second-order variations in friction that may govern fault behavior. Results of our DEM simulations demonstrate a first-order dependence of friction on grain angularity, as well as a second-order dependence on σ_n captured by equation (12), both of which may contribute to the slip behavior responsible for unstable sliding that leads to earthquakes.

[31] Several investigators have reported nonlinear friction laws similar to equation (12) that show σ_n dependence, providing a theoretical basis for our interpretation of the simulated friction data [Bowden and Tabor, 1964; Jaeger and Cook, 1976; Villaggio, 1979]. If surface deformation occurs entirely by the mechanism of elastic yielding

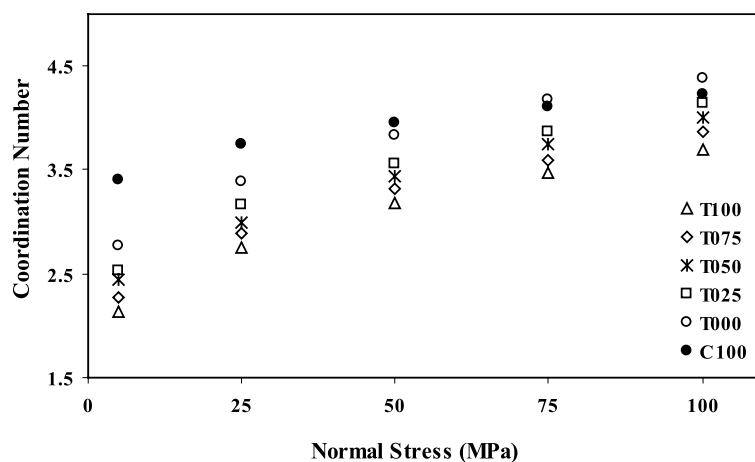


Figure 8. Average coordination number for circular particle assemblage and five-grain assemblages of different grain shape composition plotted against normal stress. Coordination numbers of all assemblages increase with decreasing grain angularity and increasing normal stress.

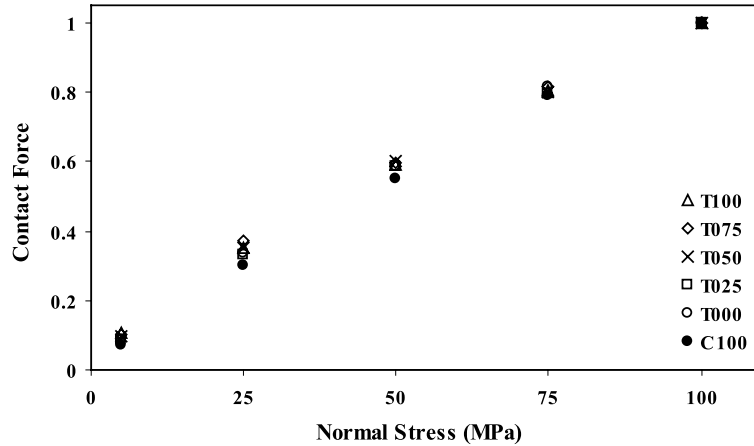


Figure 9. Average contact force for circular particle assemblage and five-grain assemblages of different grain shape composition plotted against normal stress. The average contact force is normalized by the maximum average contact force of that assemblage at 100 MPa. Normalized average contact forces increase with increasing normal stress, and their increasing rates are similar and show little dependency on the grain angularity.

of asperities, the area of contact A is proportional to $f_n^{2/3}$ according to Hertzian contact law [Mindlin and Deresiewicz, 1953; Johnson, 1985]

$$A = k f_n^{2/3} \quad (13)$$

where f_n is normal force and k is a constant related to elastic and geometrical properties of the materials. Shear force f_s can be expressed as

$$f_s = sA \quad (14)$$

where s is the shear strength of materials. Therefore friction is given by

$$\mu = f_s/f_n = s k f_n^{2/3}/f_n = s k f_n^{-1/3} \quad (15)$$

For example, friction of a diamond stylus sliding on a surface of diamond was found to follow the above friction law [Bowden and Tabor, 1964].

[32] The value for μ_{max} observed in our numerical experiments also shows an inverse power law relationship with σ_n (Figure 4). As contact forces in our simulations are calculated using the nonlinear Hertz-Mindlin contact model, our results are consistent with the above theoretical friction law. We obtain a range of power law exponents b , spanning from 0.21 to 0.40 (Table 4), which bracket the theoretical exponent of 1/3 (equation (15)). The variations in numerical values are systematic, however, indicating a strong dependence of grain shape. The exponent b is observed to increase with increasing proportion of triangular grains. This relationship suggests that the presence of nonspherical grains changes the relationship between contact force and contact area. We propose therefore that the exponent b is

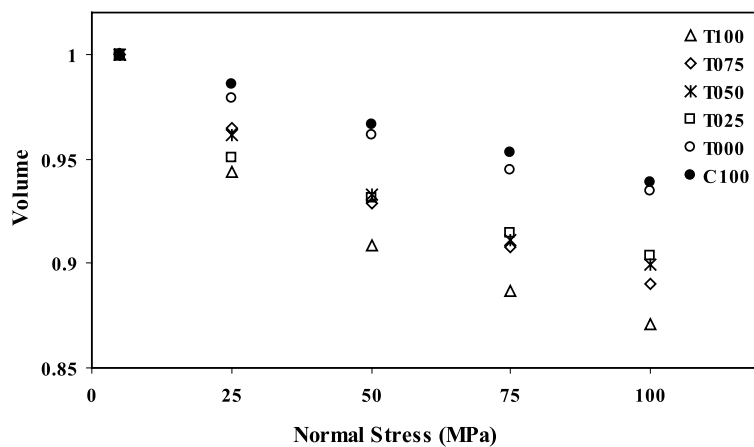


Figure 10. Average volume for circular particle assemblage and five-grain assemblages of different grain shape composition plotted against normal stress. Volume of each assemblage is normalized by the average volume of that assemblage at 5 MPa. Normalized average volumes decrease with increasing normal stress, and their decreasing rates increase with increasing grain angularity.

Table 5. Best Fit Values of Coefficient a and Exponent b for Experimental Sliding Friction of Gouges With Different Mineral Compositions

Gouge	a	b	R^2
Smectite	1.138	0.5372	0.9158
50% Smectite/50% Quartz	1.1782	0.3688	0.9666
Illite	0.8185	0.1335	0.9062
Quartz	0.8327	0.0762	0.7959

also a function of grain shape. For the same reason, the constant k also appears to change with normal force in our simulations. To summarize the effect of grain shape on μ_{\max} , we derive the following friction law based on the best fit values of coefficient a and exponent b in Table 4.

$$\mu_{\max} = (2.244S + 0.687)\sigma_n^{-(0.2075+0.244)} \quad (16)$$

where S is the proportion of triangular grains in range of 0 to 100%. This friction law encapsulates the dual dependence of μ_{\max} on both σ_n and grain shape. It shows that μ_{\max} decreases with increasing σ_n in a power form, and grain shape determines rate of change by increasing both the coefficient and exponent of the friction law.

[33] The decreasing trend of rock friction with increasing σ_n has been observed in many laboratory experiments conducted under a wide range of normal stresses [e.g., Maurer, 1965; Murrell, 1965; Byerlee, 1967, 1968; Handin, 1969; Jaeger, 1970; Edmond and Murrell, 1971; Saffer et al., 2001; Saffer and Marone, 2003]. In particular, Saffer and Marone [2003] reported on the coefficient of sliding friction of a series of direct shear experiments conducted on gouge materials of different compositions, i.e., quartz, smectite powder, smectite-quartz mixtures, and natural illite shale over a range of normal stresses from 5 to 150 MPa. Their results also show a strong second-order dependency of sliding friction on σ_n for all the gouge materials, in an

inverse power form (Figure 11). For the direct comparison between experimental observations and the numerical friction law (equation (16)), we plot equation (16) in Figure 11 for a fault gouge composed of 50% triangular grains and 50% rounded grains. Therefore a value of 0.5 is assigned to the parameter S , and the coefficient and exponent of the numerical friction law are 1.81 and 0.35, respectively. The decreasing trend of sliding friction predicted by the numerical friction law is comparable in form to those of smectite and smectite-quartz mixture, and yields predicted sliding friction values close to these of quartz and illite.

[34] Compared to the best fit values of coefficients and exponents for numerical sliding friction (Table 4), the best fit coefficients for the experimental data fall into a narrower range from 0.83 to 1.14, while the best fit exponents define a wider range from 0.08 to 0.54 (Table 5). Clearly, both the exponent and coefficient vary as a function of clay mineral abundance and composition, introducing first-order variation in experimental sliding friction that we have not simulated. No specific data are available to examine the role of grain shape in the variation of these parameters, or to make direct comparisons between numerical and experimental results of the first-order effect of grain angularity. However, alignment of platy clay minerals is suggested to be a key factor controlling the strength of clay-rich gouges [Lupini et al., 1981; Chester and Logan, 1987; Saffer et al., 2001; Saffer and Marone, 2003]. Therefore variations in the best fit coefficient and exponent for the experimental sliding friction, particularly at low stresses, may be a function of preferred clay grain orientation.

[35] The first-order variations of friction due to grain angularity observed in our numerical simulations are consistent with the observations made from laboratory experiments [Mair et al., 2002]. Our data also show the second-order dependency of friction on σ_n comparable to the recent laboratory results [Saffer et al., 2001; Saffer and Marone, 2003]. Both effects of σ_n and grain angularity on friction can be defined by an inverse

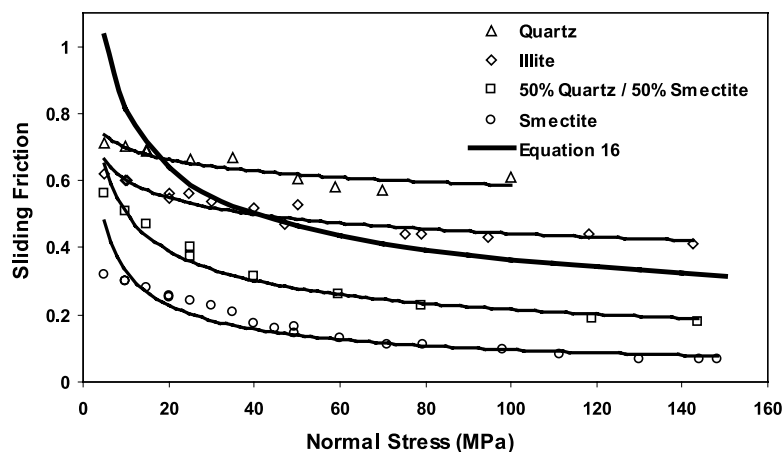


Figure 11. Comparison between experimental sliding friction [from Saffer and Marone, 2003] and sliding friction predicted by the numerical friction law (equation (16)). The decreasing trends of experimental sliding frictions are fitted in an inverse power law form. Equation (16) is plotted by assuming that fault gouge is composed of 50% triangular grains and 50% rounded grains, i.e., $S = 0.5$.

power law (equation (16)) that is identical in form to the theoretical friction law derived from Hertzian contact model (equation (15)).

4.2. Underlying Micromechanisms

[36] The results of our numerical experiments demonstrate that the variation of μ_{\max} is a response to changes in σ_n and grain angularity, which in turn affect the micromechanical behavior of granular assemblage. Previous studies on circular particle assemblages suggested that the reduction in μ_{\max} with increased σ_n for the circular particle assemblage was due to the tighter grain packing, inhibited contact sliding, and enhanced particle rolling [Morgan, 1999]. Similar effects of σ_n on micromechanical behavior of granular assemblage are also observed in our simulations. For example, dilation is inhibited at high σ_n for all the granular assemblages (Figure 10). The coordination number also increases with σ_n (Figure 8), whereas percentage of sliding contacts is nearly constant (Figure 7). Therefore the absolute number of sliding contacts increases with σ_n . The effects of σ_n on these properties are apparently small, defining the second-order dependence of friction. Grain angularity may result in more significant variations in micromechanical behavior of the granular assemblage.

[37] Grain shape variations introduce important influences on deformation mechanisms that can affect micromechanical and frictional properties of granular assemblages. At a given σ_n , the circular particle and rounded grain assemblages achieve a tighter packing than the triangular grain assemblage, as indicated by their lower porosity (Figure 5) and higher coordination number (Figure 8); strain is more frequently localized along several rows of grains parallel to shear direction or along low-angle, oblique shear bands (Figure 5); and deformation is mainly accommodated by grain rolling and sliding, resulting in lower dilation and reduced sliding friction. This observation is consistent with previous studies [Morgan, 1999; Mair et al., 2002]. In contrast, the triangular grain assemblage is characterized by a high abundance of jostling grains, bouncing against, but barely rolling over each other due to grain interlocking; strain tends to be localized along high-angle, oblique shear bands or distributed across the whole domain; deformation is mainly accommodated by grain rotation and sliding, leading to high dilation and increased sliding friction.

[38] Our data also reproduce the first-order dependency of sliding friction on grain angularity that is observed in the laboratory experiments [Mair et al., 2002]. At a normal stress of 100 MPa, μ_{\max} of the 2-D triangular grain assemblage (0.41) is still significantly lower than typical results of 3-D laboratory experiments (around 0.6) (Figure 4). The discrepancy may be explained by differences in the abundance of gouge grains, grain size, size distribution, and boundary conditions between numerical and laboratory experiments. We have not investigated these parameters in this study. In addition, laboratory experiments on 2-D glass rods and 3-D glass beads demonstrate that 2-D friction is smaller than 3-D friction due to the lack of out-of-plane particle contacts [Frye and Marone, 2002]. Therefore numerical experiments in three dimensions [e.g., Hazzard and Mair, 2003] would need to be carried out to verify if low μ_{\max} is a result of the effect of grain dimensionality on sliding friction.

[39] Enhanced grain rolling among rounded grains has been proposed as an explanation for low macroscopic frictional strength in numerical models [Mora and Place, 1998, 1999; Morgan, 1999; Mair et al., 2002]. Our results, however, reveal a more complicated picture. The characteristics and importance of active deformation mechanisms are influenced by both σ_n and grain shape. With the exception of the experiments conducted under low normal stress of 5 MPa, all of the experiments show increased rather than decreased angles of grain rotation, and the greater abundance of rotating grains in assemblages with higher proportions of triangular grains (Figure 6). Furthermore, we see increasing angles of grain rotation and percentage of rotating grains with increasing σ_n and decreasing μ_{\max} . These differences between laboratory and numerical results may arise from differences in deformation mechanisms. In direct shear experiments on thin layers of angular quartz sand and spherical glass beads [Mair et al., 2002], normal stress of 5 MPa defines a nondestructive deformation regime (i.e., with little grain comminution), where grain rolling and sliding are dominant deformation mechanisms. Under normal stresses over 20 MPa, grain fracture becomes more important. In our simulations, however, grain fracture was not allowed, so deformation must always be accommodated by grain rolling and sliding. Therefore grain rolling, characterized by enhanced grain rotation but reduced grain translation (i.e., horizontal displacement) may be a more significant deformation mechanism in our highly angular assemblages at high normal stresses. Consequently, the low μ_{\max} of fault gouge cannot be explained simply by enhanced grain rolling due to grain shape, as previously argued by others [Mora and Place, 1998, 1999; Morgan, 1999; Mair et al., 2002].

[40] In real granular shear zones, one of the fundamental observations about fault zones is that damaged wall rocks undergo grain size reduction during cataclastic flow [Sammis et al., 1986, 1987; Scholz, 1990; Blenkinsop, 1991], and angular rock fragments are progressively rounded by abrasion [Blenkinsop, 1991; Morgan et al., 1996]. Our results have shown the significant effects of grain shape on the frictional behavior of simulated granular shear zone. Therefore continuous changes in grain shape and size during simulation, optimally, due to the natural processes of grain fracture and abrasion, should be included in numerical simulations in order to obtain a comprehensive understanding of dynamics and evolution of natural fault zones. This topic is the subject of a subsequent paper (Y. Guo and J. K. Morgan, manuscript in preparation, 2004).

5. Conclusions

[41] DEM simulations of granular shear using irregularly shaped grains composed of bonded particles show that both normal stress, σ_n and grain shape have significant effects on frictional strength of our simulated granular assemblages. Observed μ_{\max} decreases with increasing σ_n in a power law form as predicted by a theoretical friction law derived from the Hertzian contact law. This relationship can be represented by the best fit power equation (equation 16). Grain shape controls the dependence of μ_{\max} on σ_n by influencing both the coefficient and exponent of the best fit friction law.

[42] In the absence of grain fracture, the triangular grain assemblage at high normal stresses is characterized by enhanced grain rotation but reduced grain translation compared with the rounded grain assemblage. Grain interlocking is significant, causing grain jostling, higher dilation, more distributed deformation, and higher μ_{\max} . Enhanced grain rolling does reduce the macroscopic frictional strength of our simulated granular assemblages, however, grain rolling cannot adequately explain the low μ_{\max} values of the triangular grain assemblage observed at normal stress of 100MPa.

[43] **Acknowledgments.** We thank David Sparks, an anonymous reviewer and Associate Editor Teruo Yamashita for their helpful comments on the manuscript. This work was funded by National Science Foundation grants EAR-0096005 and EAR-0337757. Computing facilities were made available through the Rice Center for Computational Geophysics.

References

- Antonellini, M. A., and D. D. Pollard (1995), Distinct element modeling of deformation bands in sandstone, *J. Struct. Geol.*, *17*, 1165–1182.
- Beeler, N. M., T. E. Tullis, and J. D. Weeks (1994), The roles of time and displacement in the evolution effect in rock friction, *Geophys. Res. Lett.*, *21*, 1987–1990.
- Beeler, N. M., T. E. Tullis, and J. D. Weeks (1996), Frictional behavior of large displacement experimental faults, *J. Geophys. Res.*, *101*, 8697–8715.
- Blenkinsop, T. G. (1991), Cataclasis and processes of particle size reduction, *Pure Appl. Geophys.*, *136*, 59–86.
- Bojtár, I., and K. Bagi (1993), Numerical analysis of loose and bonded granular materials, *Mech. Mater.*, *16*, 111–118.
- Bowden, F. P., and D. Tabor (1964), *The Friction and Lubrication of Solids, Part II*, Clarendon, Oxford, UK.
- Bruno, M. S., and R. B. Nelson (1991), Microstructural analysis of the inelastic behavior of sedimentary rock, *Mech. Mater.*, *12*, 95–118.
- Burbidge, D. R., and J. Braun (2002), Numerical models of the evolution of accretionary wedges and fold-and-thrust belts using the distinct-element method, *Geophys. J. Int.*, *148*, 542–561.
- Byerlee, J. D. (1967), Frictional characteristics of granite under high confining pressure, *J. Geophys. Res.*, *72*, 3639–3648.
- Byerlee, J. D. (1968), Brittle-ductile transition in rocks, *J. Geophys. Res.*, *73*, 4741–4750.
- Byerlee, J. D. (1978), Friction of rocks, *Pure Appl. Geophys.*, *116*, 615–626.
- Byerlee, J., and R. Summers (1976), A note on the effect of fault gouge thickness on fault stability, *Int. J. Rock Mech. Min. Sci. Geomech. Abstr.*, *13*, 35–36.
- Byerlee, J., V. Mjachkin, R. Summers, and O. Voevoda (1978), Structures developed in fault gouge during stable sliding and stick-slip, *Tectonophysics*, *44*, 161–171.
- Chester, F. M., and N. G. Higgs (1992), Multimechanism friction constitutive model for ultrafine quartz gouge at hypocentral conditions, *J. Geophys. Res.*, *97*, 1859–1870.
- Chester, F. M., and J. M. Logan (1987), Composite planar fabric of fault gouge from the Punchbowl Fault, California, *J. Struct. Geol.*, *9*, 621–634.
- Cundall, P. A., and R. D. Hart (1992), Numerical modeling of discontinua, *J. Eng. Comp.*, *9*, 101–113.
- Cundall, P. A., and O. D. L. Strack (1979), A discrete numerical model for granular assemblies, *Geotechnique*, *29*, 47–65.
- Day, S. M. (1982), Three-dimensional finite difference simulation of faults dynamics: Rectangular faults with fixed rupture velocity, *Bull. Seismol. Soc. Am.*, *72*, 705–727.
- Dieterich, J. H. (1979), Modeling of rock friction: 1. Experimental results and constitutive equations, *J. Geophys. Res.*, *84*, 2161–2168.
- Donzé, F., and S. A. Magnier (1995), Formulation of a 3-D numerical model of brittle behaviour, *Geophys. J. Int.*, *122*, 790–802.
- Edmond, O., and S. A. F. Murrell (1971), Experimental observations and rock fracture at pressure up to 7 kb and the implications for earthquake faulting, *Tectonophysics*, *16*, 71–87.
- Engelder, J. T., J. M. Logan, and J. Handin (1975), The sliding characteristics of sandstone on quartz fault-gouge, *Pure Appl. Geophys.*, *113*, 69–86.
- Frye, K. M., and C. Marone (2002), The effect of particle dimensionality on granular friction in laboratory shear zones, *Geophys. Res. Lett.*, *29*(19), 1916, doi:10.1029/2002GL015709.
- Fukuyama, E., and R. Madariaga (1995), Integral equation method for plane crack with arbitrary shape in 3-D elastic medium, *Bull. Seismol. Soc. Am.*, *85*, 614–628.
- Handin, J. (1969), On the Coulomb-Mohr failure criterion, *J. Geophys. Res.*, *74*, 5343–5348.
- Hazzard, J. F., and K. Mair (2003), The importance of the third dimension in granular shear, *Geophys. Res. Lett.*, *30*(13), 1708, doi:10.1029/2003GL017534.
- Itasca Consulting Group (1999), PFC2D (Particle Flow Code in 2 Dimensions), Minneapolis, Minn.
- Iwashita, K., and M. Hakuno (1990), Modified distinct element method simulation of dynamic cliff collapse, *Struct. Eng. Earthquake Eng.*, *7*, 133–142.
- Jaeger, J. C. (1970), Behavior of closely jointed rock, *Proc. Symp. Rock Mech.*, *11th*, 57–68.
- Jaeger, J. C., and N. G. W. Cook (1976), *Fundamentals of Rock Mechanics*, Chapman and Hall, New York.
- Jirásek, M., and Z. P. Bažant (1995), Particle model for quasibrittle fracture and application to sea ice, *J. Eng. Mech.*, *121*, 1016–1025.
- Johnson, K. L. (1985), *Contact Mechanics*, Cambridge Univ. Press, New York.
- Kamer, S. L., and C. Marone (1998), The effect of shear load on frictional healing in simulated fault gouge, *Geophys. Res. Lett.*, *25*, 4561–4564.
- Kamer, S. L., and C. Marone (2001), Frictional restrengthening in simulated fault gouge: Effect of shear load perturbations, *J. Geophys. Res.*, *106*, 19,319–19,337.
- Kamer, S. L., C. Marone, and B. Evans (1997), Laboratory study of fault healing and lithification in simulated fault gouge under hydrothermal conditions, *Tectonophysics*, *277*, 41–55.
- Linker, M. F., and J. H. Dieterich (1992), Effects of variable normal stress on rock friction: Observations and constitutive equations, *J. Geophys. Res.*, *97*, 4923–4940.
- Logan, J. M., M. Friedman, N. Higgs, C. Dengo, and T. Shimamoto (1979), Experimental studies of simulated gouge and their application to studies of natural fault zones, *U.S. Geol. Surv. Open File Rep.*, *79-1239*, 305–343.
- Lupini, J. F., A. E. Skinner, and P. R. Vaughan (1981), The drained residual strength of cohesive soils, *Geotechnique*, *31*, 181–213.
- Madariaga, R., K. B. Olsen, and R. J. Archuleta (1997), 3-D finite-difference simulation of a spontaneous rupture, *Seismol. Res. Lett.*, *68*, 312.
- Mair, K., and C. Marone (1999), Friction of simulated fault gouge for a wide range of velocities and normal stresses, *J. Geophys. Res.*, *104*, 28,899–28,914.
- Mair, K., and C. Marone (2000), Shear heating in granular layers, *Pure Appl. Geophys.*, *157*, 1847–1866.
- Mair, K., K. M. Frye, and C. Marone (2002), Influence of grain characteristics on the friction of granular shear zones, *J. Geophys. Res.*, *107*(B10), 2219, doi:10.1029/2001JB000516.
- Marone, C., and C. H. Scholz (1988), The depth of seismic faulting and the upper transition from stable to unstable slip regimes, *Geophys. Res. Lett.*, *15*, 621–624.
- Marone, C., and C. H. Scholz (1989), Particle-size distribution and microstructures within simulated fault gouge, *J. Struct. Geol.*, *11*, 799–814.
- Maurer, W. C. (1965), Shear failure of rock under compression, *Soc. Pet. Eng. J.*, *5*, 167–176.
- Mindlin, R. D., and H. Deresiewicz (1953), Elastic spheres in contact under varying oblique forces, *Trans. ASMEJ. Appl. Mech.*, *20*, 327–344.
- Moore, D. E., R. Summers, and J. D. Byerlee (1988), Relationship between textures and sliding motion of experimentally deformed fault gouge: Application to fault zone behavior, in *Key Questions in Rock Mechanics*, edited by P. A. Cundall, R. L. Sterling, and A. M. Starfield, *Proc. U.S. Symp. On Rock Mech.*, *29th*, 103–110.
- Mora, P., and D. Place (1998), Numerical simulation of earthquake faults with gouge: Toward a comprehensive explanation for the heat flow paradox, *J. Geophys. Res.*, *103*, 21,067–21,089.
- Mora, P., and D. Place (1999), The weakness of earthquake faults, *Geophys. Res. Lett.*, *26*, 123–126.
- Morgan, J. K. (1999), Numerical simulations of granular shear zones using the distinct element method: 2. Effects of particle size distribution and interparticle friction on mechanical behavior, *J. Geophys. Res.*, *104*, 2721–2732.
- Morgan, J. K., and M. S. Boettcher (1999), Numerical simulations of granular shear zones using the distinct element method: 1. Shear zone kinematics and the micromechanics of localization, *J. Geophys. Res.*, *104*, 2703–2719.
- Morgan, J. K., T. T. Cladouhos, K. M. Scharer, D. S. Cowan, and P. Vrolijk (1996), Fractal particle size distributions in Death Valley fault zones: Controls on mechanics and kinematics of fault rocks, *Eos Trans. AGU*, *77*(46), Fall Meet. Suppl., F717.

- Murrell, S. A. F. (1965), The effect of triaxial stress systems on the strength of rocks at atmospheric temperatures, *J. Geophys. R. Astron. Soc.*, *10*, 231–281.
- Nakatani, M. (1998), A new mechanism of slip weakening and strength recovery of friction associated with mechanical consolidation of gouge, *J. Geophys. Res.*, *103*, 27,239–27,256.
- Nakatani, M. (2001), Conceptual and physical clarification of rate and state friction: Frictional sliding as a thermally activated rheology, *J. Geophys. Res.*, *106*, 13,347–13,380.
- Nakatani, M., and H. Mochizuki (1996), Effects of shear stress applied to surfaces in stationary contact on rock friction, *Geophys. Res. Lett.*, *23*, 869–872.
- Olsen, M. P., C. H. Scholz, and A. Léger (1998), Healing and sealing of a simulated fault gouge under hydrothermal conditions: Implications for fault healing, *J. Geophys. Res.*, *103*, 7421–7430.
- Perrin, G., J. R. Rice, and G. Zheng (1995), Self-healing slip pulse on a frictional surface, *J. Mech. Phys. Solids*, *43*, 1461–1495.
- Place, D., and P. Mora (2000), Numerical simulation of localization phenomena in a fault zone, *Pure Appl. Geophys.*, *157*, 1821–1845.
- Plesha, M. E., and E. C. Aifantis (1983), On the modeling of rocks with microstructure, *Proc. U.S. Symp. Rock Mech.*, *24th*, 27–35.
- Reinen, L. A., J. D. Weeks, and T. E. Tullis (1994), The frictional behavior of lizardite and antigorite serpentinites: Experiments, constitutive models, and implications for natural faults, *Pure Appl. Geophys.*, *143*, 317–358.
- Rice, J. R., and A. L. Ruina (1983), Stability of steady frictional slipping, *J. Appl. Mech.*, *50*, 343–349.
- Richardson, E., and C. Marone (1999), Effects of normal force vibrations on frictional healing, *J. Geophys. Res.*, *104*, 28,859–28,878.
- Ruina, A. (1983), Slip instability and state variable friction laws, *J. Geophys. Res.*, *88*, 10,359–10,370.
- Saffër, D. M., and C. Marone (2003), Comparison of smectite- and illite-rich gouge frictional properties: Application to the updip limit of the seismogenic zone along subduction megathrusts, *Earth and Plan. Sci. Lett.*, *215*, 219–235.
- Saffër, D. M., K. M. Frye, C. Marone, and K. Mair (2001), Laboratory results indicating complex and potentially unstable frictional behavior of smectite clay, *Geophys. Res. Lett.*, *28*, 2297–2300.
- Sammis, C. G., R. H. Osborne, J. L. Anderson, M. Banerdt, and P. White (1986), Self-similar cataclasis in the formation of fault gouge, *Pure Appl. Geophys.*, *124*, 53–78.
- Sammis, C. G., G. King, and R. Biegel (1987), The kinematics of gouge deformation, *Pure Appl. Geophys.*, *125*, 777–812.
- Scholz, C. H. (1990), *The Mechanics of Earthquakes and Faulting*, Cambridge Univ. Press, New York.
- Scholz, C. H., M. Wyss, and S. W. Smith (1969), Seismic and aseismic slip on the San Andreas fault, *J. Geophys. Res.*, *74*, 2049–2069.
- Scholz, C. H., P. Molnar, and T. Johnson (1972), Detailed studies of frictional sliding of granite and implications for the earthquake mechanism, *J. Geophys. Res.*, *77*, 6392–6406.
- Tang, C. A. (1997), Numerical simulation of rock failure and associated seismicity, *Int. J. Rock Mech. Min. Sci.*, *34*, 249–262.
- Trent, B. C. (1987), The effect of micro-structure on the macroscopic behavior of cemented granular material, Ph.D. thesis, Univ. of Minn., Minneapolis.
- Tullis, T. E., M. L. Blanpied, and J. D. Weeks (1989), The velocity dependence of granite friction with and without simulated gouge, *Eos Trans. AGU*, *70*, 1302.
- Turcotte, D. L. (1986), Fractals and fragmentation, *J. Geophys. Res.*, *91*, 1921–1926.
- Villaggio, P. (1979), An elastic theory of coulomb friction, *Arch. Rational Mech. Anal.*, *70*, 135–143.
- Zubelwicz, A., and Z. P. Bazant (1987), Interface element modeling of fracture in aggregate composites, *J. Eng. Mech.*, *113*, 1619–1630.

Y. Guo and J. K. Morgan, Department of Earth Science, MS-126 Rice University, 6100 Main Street, Houston, TX 77005, USA. (yonggui@rice.edu)